Earthquake rupture characteristics along a developing transform boundary

J.S. Neely [1,2] Y. Huang[2] and W. Fan[3]

[1]*Department of Earth and Planetary Sciences, Northwestern University, Evanston, IL, USA. E-mail: james@earth.northwestern.edu*
[2]*Department of Earth and Environmental Sciences, University of Michigan, 500 S State St, Ann Arbor, MI 48109, USA*
[3]*Department of Earth, Ocean, & Atmospheric Science, Florida State University, 600 W College Ave, Tallahassee, FL 32306, USA*

SUMMARY

The 280-km-long San Cristobal Trough (SCT), created by the tearing of the Australia plate as it subducts under the Pacific Plate near the Solomon and Vanuatu subduction zones, has hosted strike-slip earthquake sequences in 1993 and 2015. Both sequences, which likely represent a complete seismic cycle, began along the oldest section of the SCT—the portion farthest from the tear that has experienced the most cumulative displacement—and migrated to the younger sections closer to the tear. The SCT's abundant seismicity allows us to study transform boundary development—a process rarely observed along a single fault system—through observations of earthquake rupture properties. Using the spectral ratio method based on empirical Green's functions (EGFs), we calculate the corner frequencies of three $M_w \sim 7$ 2015 earthquakes and colocated smaller earthquakes. We utilize two different spectral ratio stacking methods and fit both Brune and Boatwright models to the stacked spectral ratios. Regardless of stacking methods and spectral models, we find that the corner frequencies of the 2015 $M_w \sim 7$ earthquakes decrease slightly with distance from the tear. Assuming a constant rupture velocity and an omega-square spectral model, this corner frequency decrease may be due to an increase in rupture length with distance from the tear. The spectrum of the 2015 earthquake farthest from the tear also deviates from the omega-square model, which may indicate rupture complexity. Stress drop estimates from the corner frequencies of the 2015 $M_w \sim 7$ earthquakes range between 1 and 7 MPa, whereas stress drop estimates of their EGFs range from ~ 0.05 to 10 MPa with most values between 0.1 and 1 MPa. Independent evidence from a second moments analysis of the 2015 earthquake sequence also indicates a possible increase in rupture length with distance from the tear, confirming the results from the spectral ratio analysis. We also observe an increase in normalized centroid time-delay values, a first-order proxy for rupture behaviour, with distance from the tear for the 2015 sequence. A similar trend for the 1993 sequence suggests that earthquake rupture varies systematically along the SCT. Since distance from the tear corresponds to cumulative fault displacement, these along-strike rupture variations may be due to a displacement-driven fault maturation process.

Key words: Earthquake source observations; Spectral ratio method; Empirical Green's functions; Second moments analysis; Centroid time-delay; Transform faults.

1 INTRODUCTION

Transform boundary maturation is primarily a displacement-driven process. Increasing cumulative displacement leads to strain localization as fault strands align and lengthen and the number of fault steps decreases (Wesnousky 1988; Ben-Zion & Sammis 2003; Wechsler *et al.* 2010). Although the structural evolution of transform boundaries has been studied in both the lab (Davidesko *et al.* 2014) and the field (Martel *et al.* 1988), relatively little is known

about the seismicity associated with the maturation process. Wesnousky (1988) proposed that seismicity on a fault should reflect its current stage of structural maturation, but the long timescale of the maturation process makes this difficult to observe. Historical records show that larger transform fault earthquakes ($M_w \sim 8$) tend to occur on more mature fault systems such as the San Andreas and North Anatolian strike-slip faults, whereas seismicity along incipient strike-slip faults consists primarily of earthquake swarms (Thomas *et al.* 2013). There are few instrumental observations,
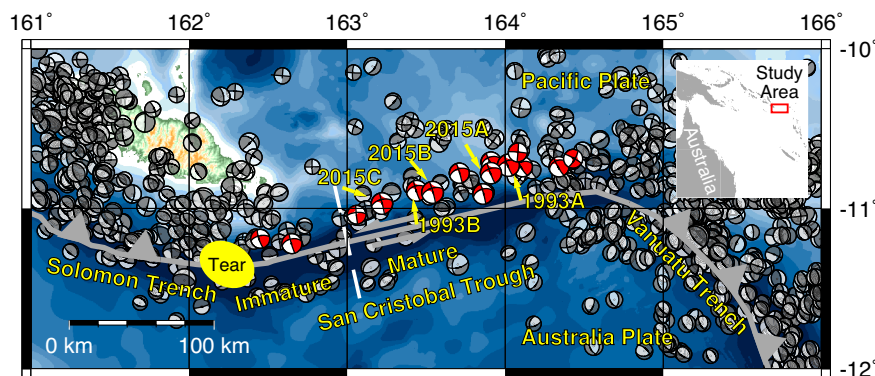
Figure 1. San Cristobal Trough (SCT) tectonic setting and local earthquake focal mechanisms. The red focal mechanisms indicate M_w 6 + strike-slip earthquakes along the SCT shown in Fig. 10. The 1993 and 2015 sequences (labeled) likely ruptured similar portions of the mature SCT.

however, of the complete maturation process along a single fault system.

Subduction Transform Edge Propagator (STEP) faults—transform boundaries created by tearing subducting plates (Govers & Wortel 2005)—provide an excellent opportunity to study transform fault development. Along a STEP fault, distance from the tear corresponds to the cumulative displacement experienced by the tearing plate. This distance-displacement relationship allows us to observe the effect of the long-term (millions of years) maturation process on seismicity without similarly long observation times. Over 24 STEPs exist globally, including the transforms at the northern and southern ends of the Lesser Antilles Trench and the transform at the northern end of the Tonga Trench (Bilich *et al.* 2001; Govers & Wortel 2005).

Although most STEPs have generally low seismicity rates (Bilich *et al.* 2001), the 280-km-long San Cristobal Trough (SCT) STEP in the southwest Pacific Ocean has produced more than 145 M_w 5+ earthquakes since 1976, providing a rich data set to study transform boundary maturation. The high seismicity is partially due to the fast relative plate motion rate (9.5 cm yr^{-1}, DeMets *et al.* 2010). The east–west striking SCT separates the Solomon and Vanuatu subduction zones where the tearing Australia plate subducts underneath the Pacific Plate (Fig. 1). Along-strike cumulative displacement, ranging from 0 to 280 km west to east, influences the SCT's earthquake behaviour and creates two distinct zones of seismicity. The western SCT rarely experiences earthquakes larger than M_w 6, whereas the eastern two-thirds has hosted several M_w ∼7 strike-slip earthquakes. Using *b*-value and Coulomb Failure Stress analyses, Neely & Furlong (2018) showed that a displacement-driven fault maturation process explains the SCT's variable seismicity. They argued that the tearing of the Australia plate creates a poorly defined plate boundary along the western SCT with short fault segments not aligned with the overall plate motion. After ∼90 km of cumulative displacement, smaller faults coalesce into larger segments oriented with plate motion that are capable of hosting M_w ∼7 earthquakes. They proposed that these two distinct seismicity zones represent immature (western third) and mature (eastern two-thirds) portions of the SCT (Fig. 1).

The mature SCT's M_w ∼7 strike-slip earthquakes are shallow (<20 km) and often occur in east-to-west propagating sequences that fail to rupture into the immature SCT (Fig. 1, Table 1). A 1993 sequence started with an M_w 7.1 (1993A 6 March 1993 03:05:49) strike-slip earthquake followed by an M_w 6.7 (1993B 6 March 1993 16:26:56) event with a similar focal mechanism. A comparable pattern occurred in 2015, which included an M_w 6.8 earthquake (2015A

Table 1. 1993 and 2015 propagating strike-slip earthquake sequences.

Event	Magnitude	Centroid distance from tear (km)	Hours since prior EQ in sequence
1993A	7.1	202	–
1993B	6.7	136	13
2015A	6.8	188	–
2015B	6.9	145	47
2015C	6.8	110	2

20 May 2015 22:48:53) followed by M_w 6.9 (2015B 22 May 2015 21:45:19) and M_w 6.8 (2015C 22 May 2015 23:59:33) earthquakes. The 1993 and 2015 propagating earthquake sequences ruptured similar portions of the SCT and may indicate a complete seismic cycle, a process that has rarely been observed instrumentally.

In this paper, we explore the source properties including corner frequency, rupture area and stress drop of the SCT's M_w ∼7 strike-slip earthquakes and their EGFs using earthquake source spectra, second moments analysis and centroid time-delays (Eshelby 1957; Madariaga 1976; Silver 1983; Pérez-Campos *et al.* 2003; Duputel *et al.* 2013). We show that the corner frequency estimates decrease slightly whereas rupture length and normalized centroid time-delays increase with distance from the tear, possibly indicating a displacement-driven maturation process within the mature portion of the SCT.

2 CORNER FREQUENCY ESTIMATES OF THE 2015 EVENTS

Earthquake source spectra, specifically the corner frequency (Aki 1967), help identify possible differences in the earthquake rupture area and stress drop. The corner frequency (f_c), where the spectrum begins to fall off, is inversely proportional to the width of the source–time function (Shearer 2009). Generally speaking, an increase in earthquake magnitude should lead to a decrease in corner frequency. To estimate corner frequencies, we utilize the spectral ratio method based on EGFs. This method isolates the source component from the path and site effects by deconvolving the seismogram of the master event by the seismogram of a smaller, colocated EGF event (Mueller 1985; Ide *et al.* 2003; Imanishi & Ellsworth 2006; Baltay *et al.* 2010; Abercrombie 2015, Fig. 2). We perform the spectral ratio analysis on the 2015 strike-slip sequence. We attempted a similar analysis for the 1993 sequence, but the limited station coverage at the time provides few useful measurements.
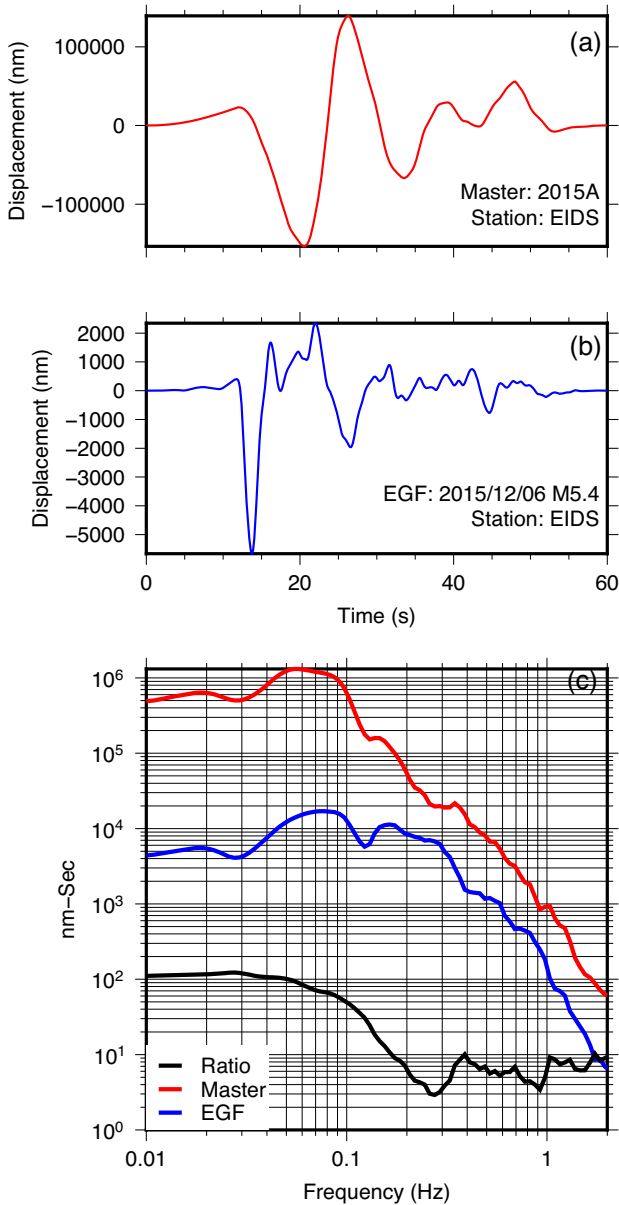
a five-point moving average window to smooth the spectra (Imanishi & Ellsworth 2006). The resampling produces four times the number of data points between 0.01 and 0.1 Hz (the likely master corner frequency range) than between 1 and 2 Hz. We require an EGF's signal-to-noise ratio to be >2 in two frequency bands—0.01–0.1 Hz and 0.1–1 Hz. These bands approximately encompass the master corner frequencies and EGF corner frequencies, respectively. We compare the 60-s-long signal window to the preceding 60 s for the signal-to-noise ratio test. We divide the master spectra by the EGF spectra to cancel out path and site effects and obtain the source spectral ratios.

We stack master–EGF spectral ratios with two approaches. The first approach stacks spectral ratios over multiple stations per EGF (hereinafter called EGF stack). The requirement of master–EGF pairs with strong signals at two or more stations leads to 14 EGFs (5 each for 2015A and 2015B, 4 for 2015C) and 60 spectral ratios. We first compute the geometric mean of the spectral amplitudes over stations per EGF, which preserves the corner frequency of the EGF. A representative master event corner frequency is then computed by taking the geometric mean of the corner frequencies from the EGF stacks. The second method stacks spectral ratios of all master–EGF pairs across all stations per master event (hereinafter called full stack), which can potentially reduce the variabilities in corner frequency caused by different EGFs and compensate for limited station coverage (Abercrombie 2015). We normalize the spectral ratios before stacking to preserve the master event corner frequency information only and then compute the geometric mean of all spectral ratios for each master event. This full stack method incorporates 29 unique EGFs (Table S1) and 77 spectral ratios.

We estimate the master event's corner frequency (f_c^M) by fitting the Brune ($g = 1$, Brune 1970) and Boatwright models ($g = 2$, Boatwright 1980) to the stacked spectral ratios:

$$\frac{u_M(f)}{u_{EGF}(f)} = \frac{M_o^M}{M_o^{EGF}} \left(\frac{1 + \left(\frac{f}{f_c^{EGF}}\right)^{2g}}{1 + \left(\frac{f}{f_c^M}\right)^{2g}} \right)^{1/g}. \tag{1}$$

Both models assume a falloff exponent of 2, but the Boatwright model has a sharper corner than the Brune model. The inversion solves for the moment ratio (M_o^M/M_o^{EGF}), master (f_c^M) and EGF corner frequency (f_c^{EGF}) (trust-region-reflective optimization, MATLAB 2015a). When modeling the stacked spectral ratio, we take two key steps to ensure a better fit. First, we use an upper frequency bound of 2 Hz. This ensures that the minimization algorithm focuses mainly on the signal around the master and EGF corner frequencies and is not unduly influenced by high-frequency noise. Secondly, we perform the model fitting in log space [i.e. $\log_{10}(u_M(f)/u_{EGF}(f))$] to prevent the large residuals at low frequencies in linear space from dominating the fit. A bootstrap analysis allows for estimation of the corner frequency uncertainties and produces a Gaussian distribution of model parameters (Huang *et al.* 2016). For the bootstrap analysis, we randomly sample the residuals with replacement and add the resampled residuals to the measured spectral ratio to create a synthetic spectral ratio. We estimate source parameters for the synthetic spectral ratio and repeat this process 1000 times.

Synthetic tests of the full stack method indicate that the stacking method preserves the master event corner frequency if the EGF corner frequencies are within ~1 order of magnitude of each other (Fig. S1). We create idealized spectral ratios with the same master corner frequency but different EGF corner frequencies and
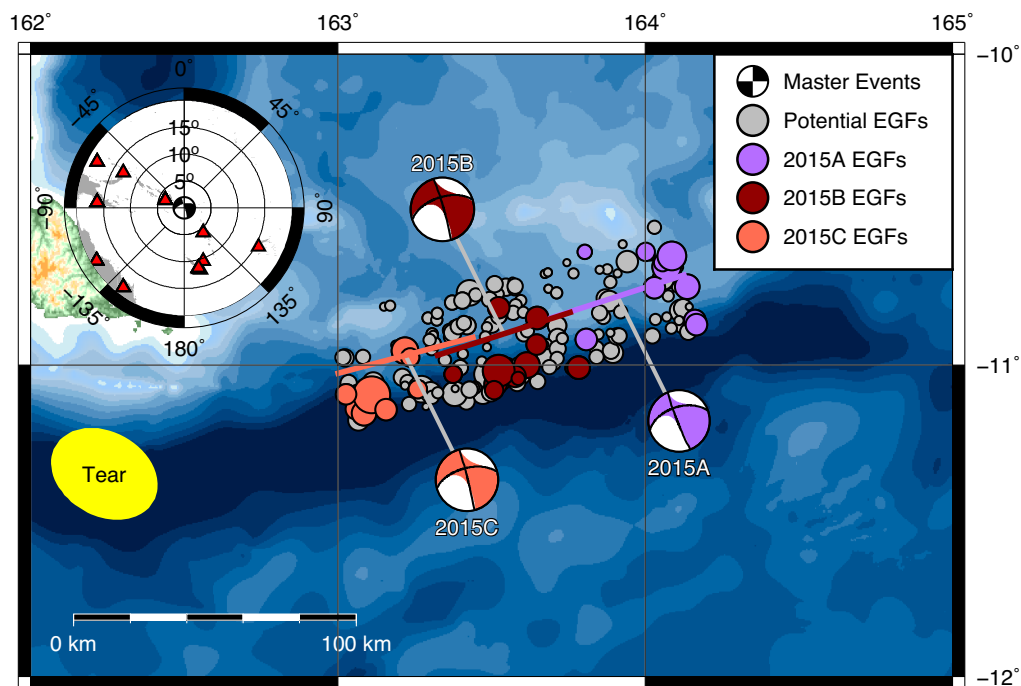

Figure 2. Processing steps for spectral ratio method via EGF. We perform a fast Fourier transform on the master (a) and a collocated EGF (b) seismograms. We divide the master amplitude frequency spectrum by the EGF amplitude frequency spectrum to produce the spectral ratio (c).

We assume a 50 km rupture extent (Wells and Coppersmith 1994) centered on the centroid location of the master event (this assumes a bilateral rupture). We select EGFs ($M_w < 6$) located within 20 km of this assumed rupture extent (Fig. 3). These selection criteria assume ideal EGFs are within one source dimension of the master event (Abercrombie 2015), yielding 214 potential EGFs. We first convert the velocity seismograms (in counts) to displacement and then calculate *P*-wave displacement spectra using a 60-s-long window that begins 12 s before the direct *P*-wave arrival on the vertical component of 15 broad-band stations between ~3° and 20°. This windowing ensures clean *P* waves and avoids contaminations from *S* or surface waves at all stations. We then resample the individual amplitude spectra in log space with a 0.025 $\log_{10}$(Hz) increment spacing to sample the lower frequencies more frequently and apply

Figure 3. Station coverage and EGF distribution for the 2015 sequence. The focal mechanisms indicate the 2015 master events. Colored lines indicate assumed rupture lengths corresponding to three master events. Grey circles indicate potential EGFs that did not pass the SNR test. Colored circles show EGFs utilized in the spectral ratio analysis. The inset shows the stations (red triangles) used in this analysis.

moment ratios, and add noise (sampled from a log-normal distribution) to the idealized spectral ratios to create synthetic ones. The full stack methodology is then used to average the synthetic spectral ratios over different master–EGF pairs. The full stack synthetic spectral ratios are modeled to check how the addition of noise impacts our ability to resolve the true corner frequency value. Although the stacked spectral ratio loses information regarding the individual EGFs, the master corner frequency can be recovered.

The EGF and full stack methods produce consistent corner frequency values for each of the 2015 M_w ∼7 earthquakes (Figs 4 and 5). Despite the variability associated with individual EGFs in the EGF stack method, the geometric mean of corner frequencies for 2015C is slightly higher (∼0.06 Hz) while it is similar for 2015A and 2015B (∼0.05 Hz, Fig. 4). Using the full stack method, we find that 2015C has the highest corner frequency (∼0.07 Hz) followed by 2015B (∼0.06 Hz) and 2015A (∼0.05 Hz) (Fig. 5). Consistent corner frequency values are obtained from the Brune and Boatwright spectral models given the 2σ bootstrap uncertainty of ∼0.005–0.01 Hz (Fig. 5). While some studies see negligible differences between the Brune and Boatwright corner frequencies (Baltay *et al.* 2011; Abercrombie 2014; Huang *et al.* 2017), others have found that the Boatwright model fits the observed spectral ratio better and leads to a lower corner frequency (Huang *et al.* 2016). The Brune and Boatwright corner frequencies for the 2015 sequence are remarkably similar. The maximum difference between the Brune and Boatwright corner frequencies for a single master event is less than 0.008 Hz. Overall, regardless of spectral model or stacking method, the geometric means of corner frequencies for the 2015 M_w ∼7 earthquakes appear to slightly decrease with distance from the tear.

Intriguingly, the spectral ratios of 2015A appear to deviate from both omega-square models and exhibit a high-frequency falloff exponent greater than 2. Although the spectral models indicate that 2015A has the lowest corner frequency, a comparison of the full stack spectra show that 2015A's low frequency plateau extends to slightly higher frequency values than either 2015B's or 2015C's low frequency plateaus (Fig. 5). Fig. 6(a) shows the ratio of observed spectra divided by the best fitting Brune model. Reds indicate regions where the Brune model underestimates the spectrum, while blues indicate frequency intervals where the model overestimates the spectrum. The Brune model significantly underpredicts the observed 2015A spectrum at frequencies above the master corner frequency before rapidly shifting to an overprediction at ∼0.1 Hz. Although the 2015B and 2015C residuals show areas of over- and underprediction, they do not exhibit such a strong reversal trend along the falloff portion of the spectra. Such deviations from the omega-square model may be due to the imperfect cancellation of propagation and site effects of master–EGF pairs. However, due to the fact that this systematic deviation is only observed for 2015A, it may also imply a more complex rupture process than the rupture considered in the omega-square model (Uchide and Imanishi 2016). We test how this deviation from the omega-square model may affect the corner frequency estimate of 2015A by allowing the slope of the Brune model to vary freely. We find a best-fitting falloff exponent of ∼5 and a corner frequency of ∼0.08 Hz for 2015A (Table 2), whereas a best-fitting falloff exponent of ∼2 is still valid for 2015B and 2015C (Fig. S2). By allowing the falloff exponent to vary, we see a significant reduction in the residuals for 2015A and the elimination of the systematic under- and overpredictions previously observed for the fixed falloff exponent model (Fig. 6b). We further address the implications of a complex 2015A rupture in the 'Discussion' section.
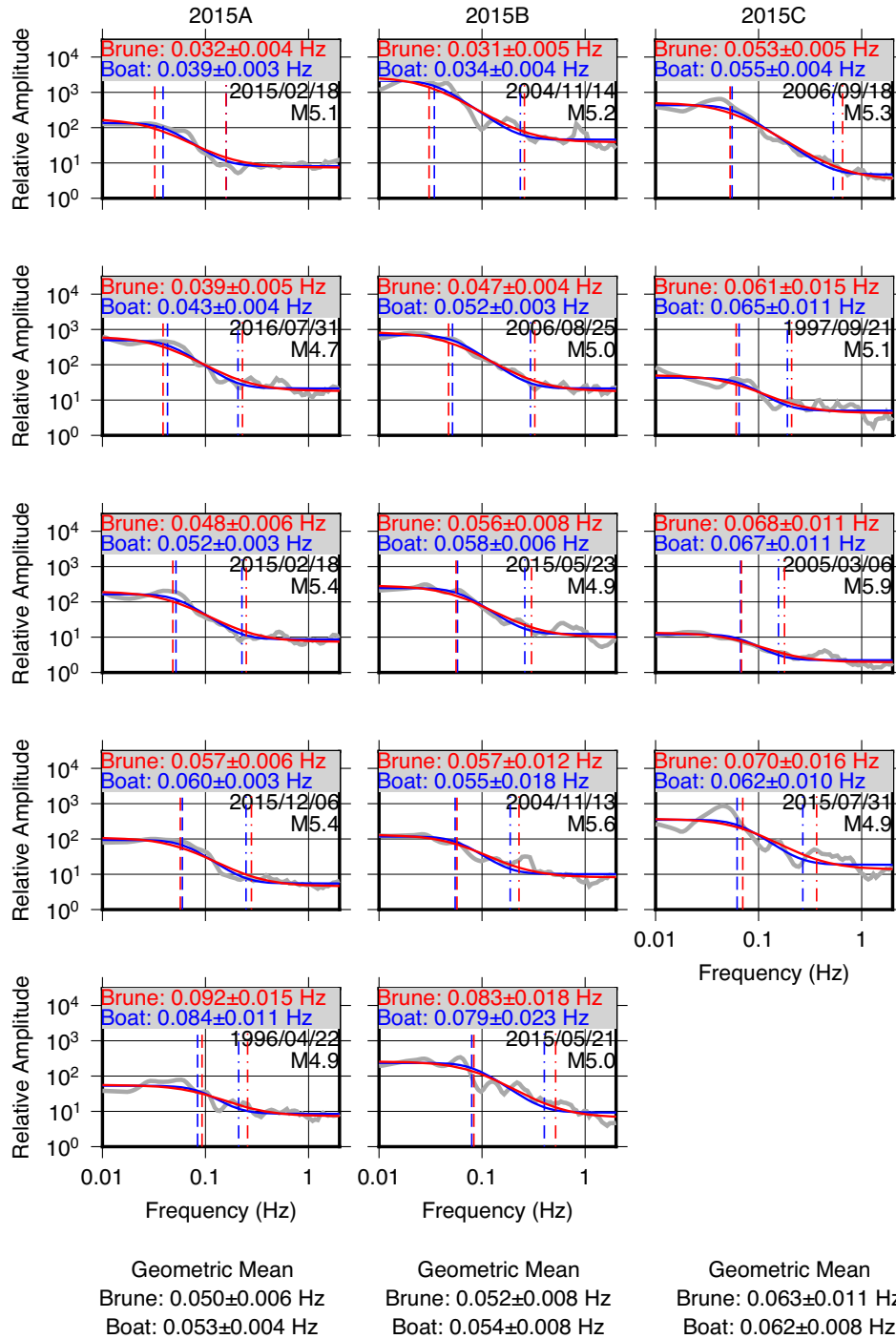
Figure 4. Spectral ratio results for the EGF stack method. Columns are grouped by the 2015 master event. Each panel includes the stacked spectral ratios (grey) with Brune (red) and Boatwright (blue) models for an EGF. Master corner frequencies with 2σ uncertainty calculated from Brune and Boatwright models are shown for each EGF. Dashed lines indicate master corner frequencies. Dotted–dashed lines indicate EGF corner frequencies. Geometric means are displayed at the bottom of the columns.

From the EGF stack method, we also obtain the EGF corner frequencies, which range from ~0.1 to ~0.6 Hz. In contrast to the master events, there are systematic differences between the corner frequencies estimated from different spectral models (Fig. 7). The Brune spectral model produces slightly higher EGF corner frequency values than the Boatwright model (Fig. 7). The corner frequency values of 2015A's EGFs are more tightly clustered than 2015B's and 2015C's EGFs, though the

magnitudes of 2015A's EGFs span a similar range as the other EGFs.

3 RUPTURE LENGTH AND STRESS DROP OF THE 2015 EVENTS

By assuming simple, symmetric circular and elliptical rupture models, we can use corner frequency estimates to determine the rupture
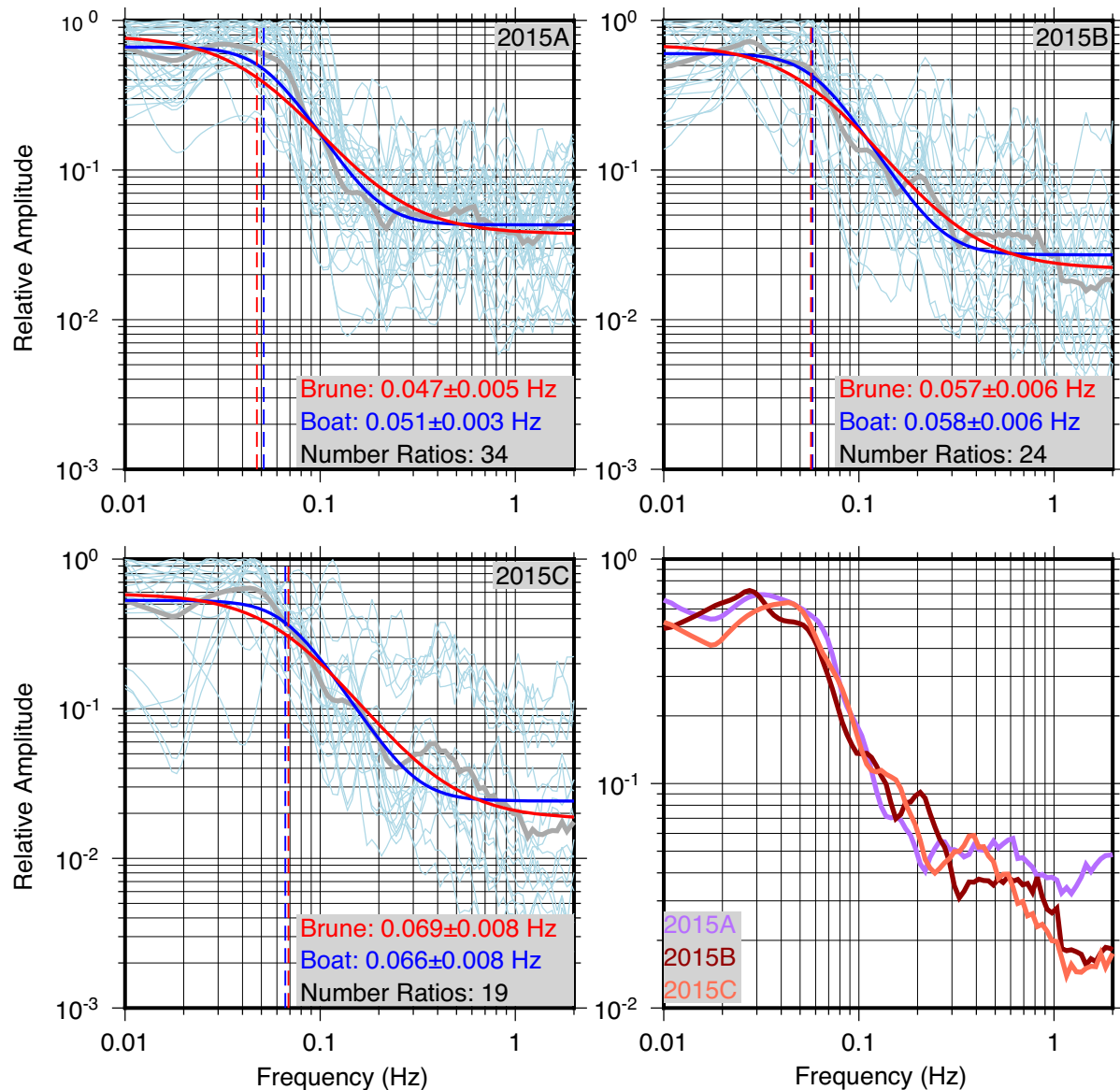
Figure 5. Spectral ratio results for the full stack method. The first three panels correspond to the 2015 earthquakes and include the stacked spectral ratios (grey), individual spectra (light blue), and modeled spectral ratios with Brune (red) and Boatwright (blue) models. Master corner frequencies (also shown with dashed lines) with 2σ uncertainty calculated from Brune and Boatwright models are listed. The number of individual spectral ratios included in the stack is also indicated. Bottom right-hand panel: all three full stack spectra are plotted together.

length and stress drop of an earthquake (Eshelby 1957; Sato & Hirasawa 1973; Madariaga 1977; Kaneko & Shearer 2015). In the circular model, the radius of rupture (a) is inversely proportional to the corner frequency (f_c) multiplied by the S-wave speed ($\beta = 3.5$ km s^{-1}) and a constant k (Eshelby 1957).

$$a = k\frac{\beta}{f_c}. \qquad (2)$$

A similar relationship also exists for elliptical rupture models where b is the seismogenic zone half width and a is half the rupture length (Kaneko & Shearer 2015).

$$a = \frac{1}{b}\left(\frac{k\beta}{f_c}\right)^2. \qquad (3)$$

Different k values have been proposed depending on the rupture model, but the value of k is traditionally calculated assuming a

rupture velocity that is 90 per cent of the S-wave velocity. We utilize k values from Kaneko and Shearer (2015), who used a cohesive-zone rupture model to numerically calculate k. If we assume a rupture velocity that is 90 per cent of the S-wave velocity, $k = 0.29$ for a symmetric circular rupture, and $k = 0.25$ for a symmetric elliptical rupture.

Fig. 8 and Table 2 show the rupture extent for the 2015 strike-slip earthquakes estimated from the Brune corner frequencies calculated from the EGF stack and full stack approaches. Assuming a circular rupture model and the same rupture velocity for the three earthquakes, we find that 2015C has the smallest rupture extent using corner frequencies from both stacking methods. The rupture area for 2015A is larger than 2015B's rupture area when calculated from the full stack corner frequencies, but they are more similar for the EGF stack method. In both cases, there is little to no overlap between the 2015 events. A similar trend of increasing rupture
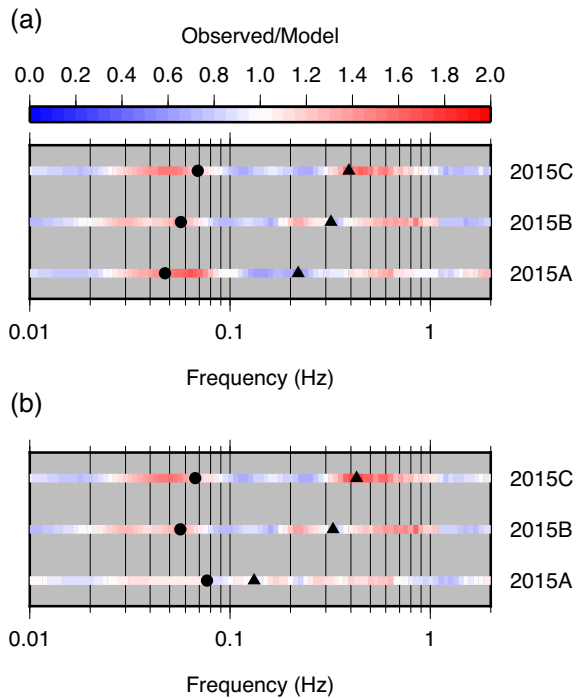
(a)

(b)

Figure 6. Ratios of observed versus Brune modeled spectral ratios of the 2015 events for the full stack method. The corner frequencies of the master events (circle) and of the EGFs (triangle) are indicated. Blue indicates model overestimation, and red indicates model underestimation. (a): Residuals for fixed falloff exponent (2) Brune model. The rapid red-to-blue transition at ∼0.1 Hz indicates a steep falloff in 2015A's observed spectral ratio. (b): Residuals when Brune model falloff exponent is allowed to vary. Note that unlike 2015B and 2015C, 2015A's residuals are significantly reduced.

areas with distance from the tear is also suggested from an elliptical rupture model. Constraining the width of the seismogenic zone along the SCT is challenging with only teleseismic data. The large earthquakes have centroid depths around 20 km but the depths of the smaller earthquakes are not well constrained. Locking depths have been reported around 20 km at mature strike-slip fault systems like the San Andreas Fault (Smith-Konter *et al.* 2011) and North Anatolian Fault (Aktuğ *et al.* 2015). Therefore, we assume a minor axis of 20 km. Though there is some overlap in the elliptical rupture areas, the 2015 earthquake centroids are at the outer edge of the upper limit of the adjoining earthquake's rupture extent. Note that a decrease in the minor axis leads to an increase in the rupture length and additional rupture overlap.

Using the rupture areas and earthquake moments, we can calculate the corresponding stress drops. For a circular fault, we determine the stress drop ($\Delta\sigma$) from the earthquake's moment (M_o) and rupture radius (a) (Eshelby 1957).

$$\Delta\sigma = \frac{7}{16}\frac{M_o}{a^3}. \tag{4}$$

For an elliptical fault, we calculate the stress drop via a shape factor (C), M_o, minor axis (b) and rupture area (S) (Madariaga 1977).

$$\Delta\sigma = \frac{M_o}{CbS}. \tag{5}$$

We calculate the shape factor (C):

$$C = \frac{4}{3E(m) + \dfrac{1}{m^2}\left(E(m) - \dfrac{b^2}{a^2}K(m)\right)} \tag{6}$$

$$m = \left(1 - \frac{b^2}{a^2}\right)^{1/2}, \tag{7}$$

where $K(m)$ and $E(m)$ are the complete elliptical integrals of the first and second kinds (Madariaga 1977).

Stress drop results are shown in Fig. 9 and Table 2. The elliptical rupture model leads to slightly larger stress drop values (2–6 MPa) than the circular rupture model (1–3 MPa) for the 2015 master earthquakes. For both rupture models, the stress drop of 2015A is lower than those of 2015B and 2015C by a factor of 2 (Fig. 9). The stress drop estimates of EGFs calculated from a circular rupture model show greater variations than the stress drop estimates of the master events and range from ∼0.05 to 10 MPa with most values between 0.1 and 1 MPa. We do not observe any discernable stress drop pattern among the different EGF groups with the current dataset. The observed EGFs variations warrant future investigations with near field observations. The range of our stress drop estimates also agrees with previous stress drop studies for large transform fault earthquakes (Allmann & Shearer 2009).

4 CENTROID TIME-DELAY OF REPEATING EARTHQUAKES

Centroid time-delay (τ_{CTD}), the difference between centroid and hypocenter times, approximates the half rupture duration of an earthquake and serves as a first-order proxy for rupture characteristics (Duputel *et al.* 2013). The centroid time-delay calculation is another tool for investigating rupture variations along the SCT. Earthquakes with a large centroid time-delay for a given moment may have anomalously large rupture areas, slow rupture velocities, or complex ruptures consisting of multiple subevents (Duputel *et al.* 2013). Earthquakes with anomalously large rupture areas or slow rupture velocities will have lower corner frequencies than complex rupture earthquakes with similar magnitudes (Pérez-Campos *et al.* 2003).

Since centroid time-delay increases with moment, we normalize it by the expected centroid time-delay (τ_r) for a given moment [Duputel *et al.* 2013, moment (M_o) in dyne-cm]:

$$\tau_r = 1.2 \times 10^{-8} \times M_o^{1/3}. \tag{8}$$

Normalized centroid time-delay values of large earthquakes range from 0.5 to 4, but most values are clustered near 1 (Duputel *et al.* 2013; Ye *et al.* 2016). Many of the outliers with abnormally large centroid time-delays occur along mid-ocean ridge transform faults (Pérez-Campos *et al.* 2003; Duputel *et al.* 2013).

We calculate centroid time-delays (using the ANSS ComCat hypocenter and GCMT centroid times) and estimate the normalized values for 15 M_w 6 + earthquakes (including the 1993 and 2015 sequences) along the SCT (Fig. 10; Table S2). We also used W-phase catalog information (http://wphase.unistra.fr and personal communication with Dr Zacharie Duputel) for the 1993 and 2015 earthquakes. We included all earthquakes greater than M_w 6 that are within 30 km of the SCT. We did not include earthquakes at the far western and eastern ends of the SCT. Events at the western end of the SCT likely represent Australia intraplate tearing and thus are

Table 2. Expected corner frequencies from centroid time-delay, estimated corner frequencies, rupture dimensions, and stress drops (with 2σ uncertainties) from the spectral ratios using Brune model and different stacking methodologies for the 2015 sequence. The elliptical model assumes a 20 km minor axis. Full stack (fixed slope) indicates a set spectrum falloff exponent of 2. In the full stack (free slope) model, we allowed the falloff exponent to vary.

|	f_c (Hz)	Circ. diam. (km)	Circ. $\Delta\sigma$ (MPa)	Ellip. length (km)	Ellip. $\Delta\sigma$ (MPa)
Event: 2015A					
Centroid time-delay	0.030	–	–	–	–
EGF stack	0.050 ± 0.006	$40.5^{+5.8}_{-4.5}$	$1.0^{+0.4}_{-0.3}$	$61.0^{+18.8}_{-12.9}$	$2.1^{+0.6}_{-0.5}$
Full stack (fixed slope)	0.047 ± 0.005	$42.8^{+4.8}_{-4.0}$	$0.9^{+0.3}_{-0.2}$	$68.1^{+16.3}_{-12.0}$	$1.8^{+0.4}_{-0.4}$
Full stack (free slope)	0.077 ± 0.003	$26.5^{+1.1}_{-1.0}$	$3.7^{+0.5}_{-0.4}$	$26.1^{+2.3}_{-2.0}$	$4.8^{+0.3}_{-0.4}$
Event: 2015B					
Centroid time-delay	0.045	–	–	–	–
EGF stack	0.052 ± 0.008	$39.0^{+7.0}_{-5.1}$	$2.0^{+1.0}_{-0.8}$	$56.4^{+22.1}_{-13.9}$	$3.8^{+1.3}_{-1.1}$
Full stack (fixed slope)	0.057 ± 0.006	$35.7^{+3.9}_{-3.2}$	$2.6^{+0.8}_{-0.7}$	$47.5^{+10.9}_{-8.1}$	$4.6^{+1.0}_{-0.9}$
Full stack (free slope)	0.057 ± 0.008	$35.9^{+6.3}_{-4.7}$	$2.5^{+1.3}_{-1.0}$	$47.8^{+18.4}_{-11.7}$	$4.5^{+1.5}_{-1.3}$
Event: 2015C					
Centroid time-delay	0.050	–	–	–	–
EGF stack	0.063 ± 0.011	$32.5^{+6.9}_{-4.9}$	$2.5^{+1.6}_{-1.1}$	$39.1^{+18.5}_{-10.8}$	$4.1^{+1.6}_{-1.3}$
Full stack (fixed slope)	0.069 ± 0.008	$29.5^{+4.0}_{-3.1}$	$3.3^{+1.3}_{-1.1}$	$32.4^{+9.4}_{-6.6}$	$4.9^{+1.2}_{-1.1}$
Full stack (free slope)	0.067 ± 0.011	$30.3^{+5.7}_{-4.2}$	$3.1^{+1.7}_{-1.2}$	$34.2^{+14.2}_{-8.7}$	$4.7^{+1.5}_{-1.4}$
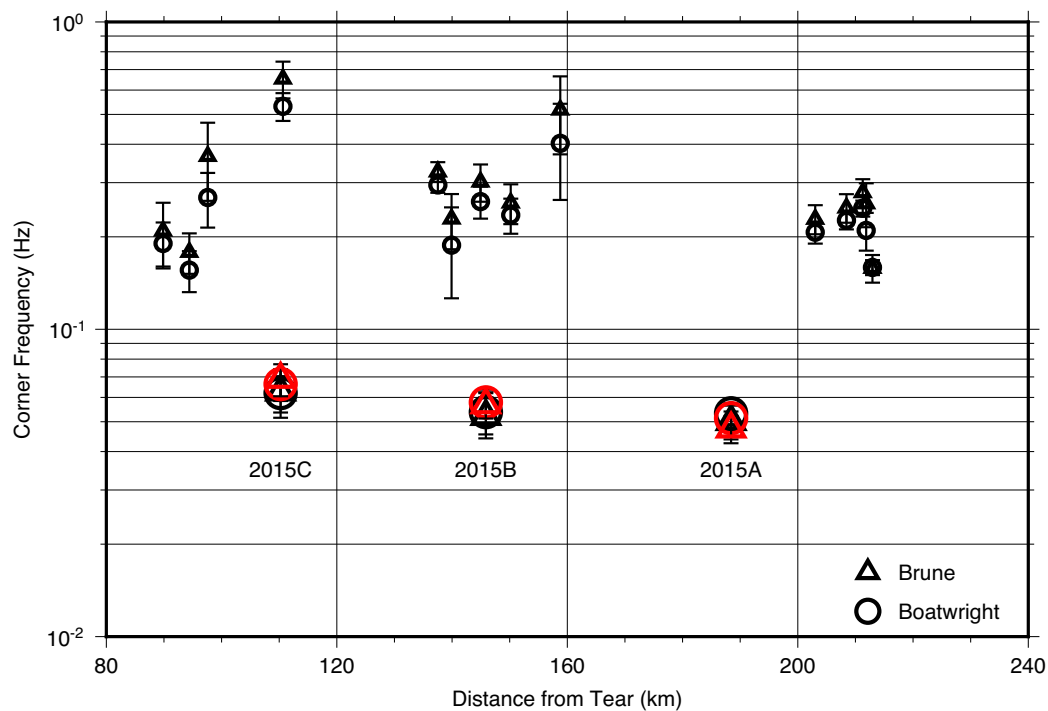
Figure 7. Corner frequency results for the 2015 events and the EGFs. Triangles and circles indicate Brune and Boatwright models, respectively. Small symbols indicate EGFs. Large symbols indicate the 2015 events. Error bars represent 2σ. Black symbols are from the EGF stack method. Red symbols indicate results from the full stack method (only applicable for the 2015 events).

not considered transform boundary seismicity (Neely & Furlong 2018). Along the far eastern end of the SCT, the adjoining Vanuatu subduction zone dominates the seismicity.

Our distance and magnitude criteria include 16 earthquakes. One of these earthquakes however has a negative centroid time-delay (M_w 6.1 27 March, 1982 GCMT_ID: 032782E) and has been excluded from the list. The 15 earthquakes included in Fig. 10 are listed in Table S2. The larger normalized centroid time-delays are generally found at the SCT's eastern end (Fig. 10). The 1993 and 2015 sequences, which contain the SCT's largest recorded earthquakes, exhibit a relative west to east increase in normalized centroid time-delay values within each sequence. The largest value in each sequence occurs at the far eastern end of the SCT. 1993B has the lowest value (0.78) followed by 2015C (0.84) and 2015B (0.85).
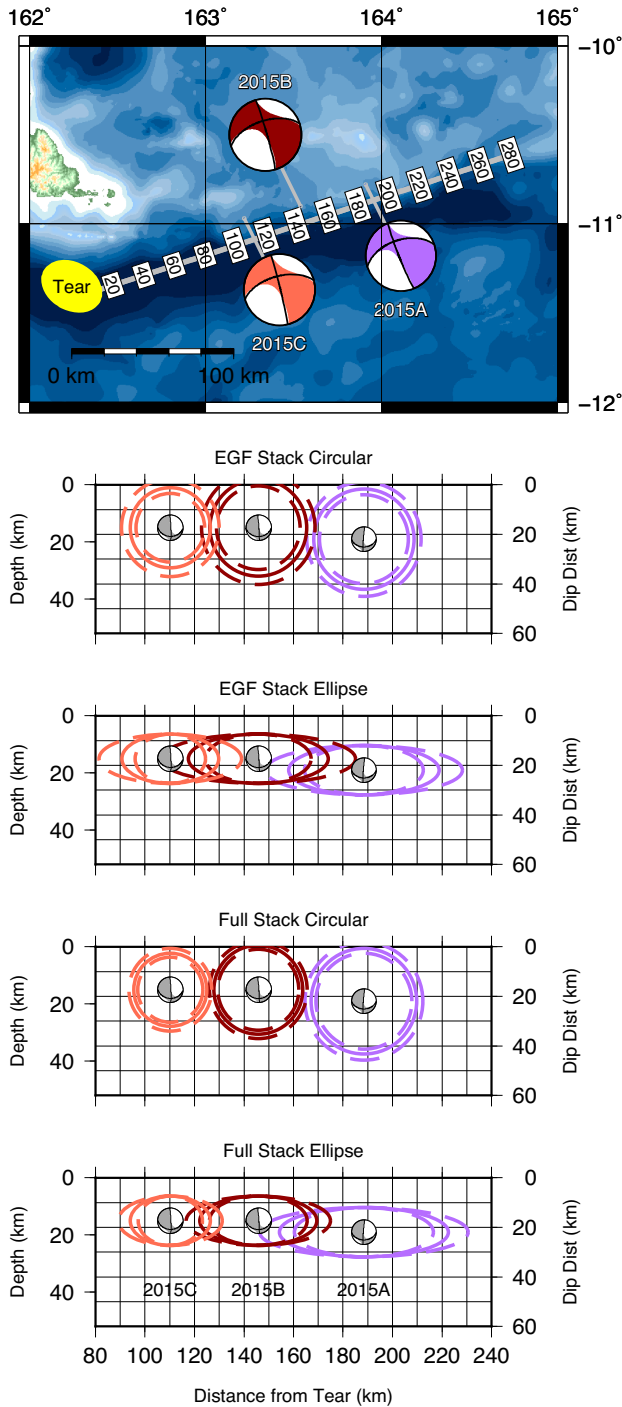
Figure 8. Rupture areas for the 2015 strike-slip earthquake sequence using the *k* values from Kaneko and Shearer (2015), assuming a constant rupture velocity. Top figure shows the three 2015 earthquakes with distance from the tear. The bottom four cross-section panels show circular and elliptical models for the EGF and full stack method results. Solid lines indicate mean rupture extent. Dashed lines indicate 2σ uncertainties.

2015A (1.52) and 1993A (1.05), the earthquakes farthest from the tear, have the largest values in their sequences, respectively. These two sequences suggest that normalized centroid time-delays may increase with distance from the tear and cumulative displacement. Normalized centroid time-delay values calculated from W-phase solutions (Duputel *et al.* 2012) for the 1993 and 2015 sequences

show the same increasing trend with distance from the tear (Fig. 10, Table S3).

The relative normalized centroid time-delay difference between 1993B (0.78) and 2015A (1.52) is one of the largest normalized centroid-time delay differences for large, similarly oriented, strike-slip earthquakes globally. A review of strike-slip earthquakes in the Duputel *et al.* (2013) data set (M_w 6.5 + earthquakes from 1990–2012) that have similar double-couple orientations (Kagan 2007) and are within 300 km of each other indicates that the Romanche Transform, offsetting the Mid-Atlantic Ridge and the Gorda plate are the only other regions with greater normalized centroid time-delay variations (Text S1). However, seismicity along mid-ocean ridge transforms such as the Romanche Transform is strongly affected by thermal structure (Abercrombie & Ekström 2001) rather than displacement-driven maturation. Additionally, the Gorda Plate earthquakes do not all occur on the plate boundary and are not likely occurring along the same suite of structures. Since the SCT has the largest normalized centroid time-delay variations among comparable transform faults, the west-to-east increase of normalized centroid time-delay along the SCT is likely not due to random perturbations. The repetition of this west-to-east increase in both the 1993 and 2015 sequences, which may represent a full seismic cycle, further suggests that we are observing systematic rupture variations indicative of underlying fault properties.

Assuming a triangular source–time function, which relates to a simple earthquake rupture rather than multiple subevents, the corner frequency can be calculated from the centroid time-delay (Duputel *et al.* 2013)

$$f_c = \frac{1}{\pi \tau_{CTD}} \ . \tag{9}$$

Based on the observed centroid time-delays for the 2015 sequence, we expect 2015A to have the lowest corner frequency while 2015B and 2015C have slightly larger values (2015A: 0.030 Hz; 2015B: 0.045 Hz; 2015C: 0.050 Hz). Note that the relative values of the predicted corner frequencies are more important than the absolute values of the predicted corner frequencies given the simple assumption of a triangular source–time function. The predicted trend of slightly decreasing corner frequency with distance from the tear, however, matches the trend observed from the spectral ratio analysis based on omega-square spectral models (Table 2). For both the predicted and observed corner frequency values, 2015A has the lowest corner frequency, and 2015C has the highest corner frequency.

5 SECOND MOMENTS ANALYSIS OF THE 2015 EARTHQUAKE SEQUENCE

We perform a second moments analysis to further investigate the rupture kinematics of the 2015 earthquake sequence. The second moments method allows for direct estimation of earthquake length, width, duration and rupture directivity without an *a priori* rupture model (e.g. Silver 1983) to reliably estimate rupture areas for diverse complex rupture scenarios (McGuire & Kaneko 2018). Knowing the local velocity structure, earthquake second moments can be estimated from a set of apparent durations for any given seismic phases:

$$\mu^{(0,2)}\left(\underline{s}\right) = \hat{\mu}^{(0,2)} - 2\underline{s} \cdot \widehat{\underline{\mu}}^{(1,1)} + \underline{s}^T \cdot \widehat{\underline{\underline{\mu}}}^{(2,0)} \cdot \underline{s}, \tag{10}$$
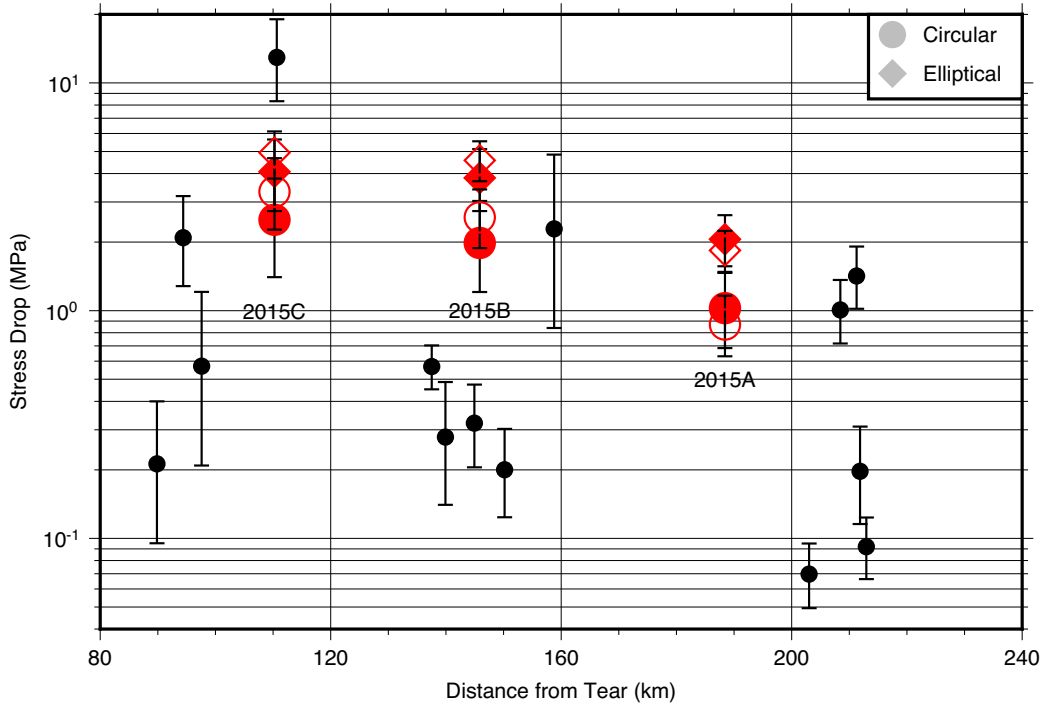
Figure 9. Stress drop results for the 2015 master events and EGFs using the Brune model. Circles indicate the circular rupture model. Diamonds indicate the elliptical rupture model (only applicable to 2015 master events). Filled shapes indicate stress drops calculated via the EGF stack model. Open shapes represent results calculated from the full stack model. Larger, red symbols are the 2015 master earthquakes. Small, black symbols indicate the EGFs. Error bars represent 2σ.
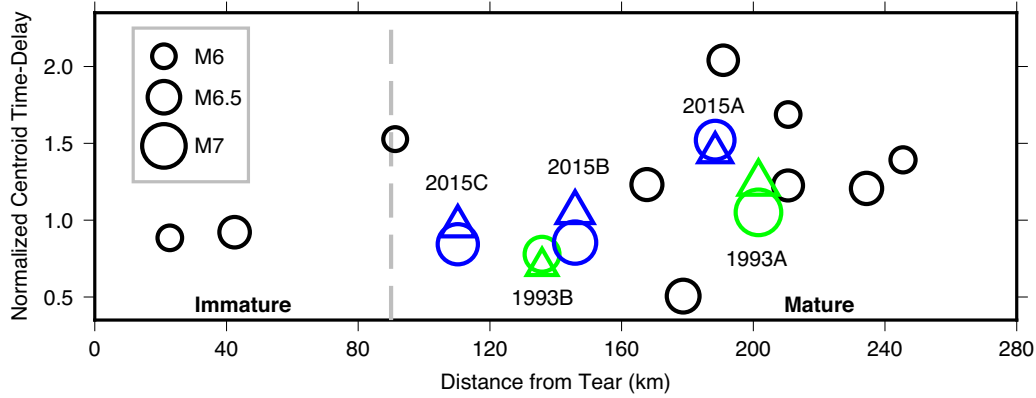

Figure 10. Normalized centroid time-delays of M_w 6 + strike-slip earthquakes (red focal mechanisms in Fig. 1) along the SCT as a function of distance from the tear. Circles show GCMT derived data. Triangles are W-phase derived data. 1993 (green) and 2015 (blue) sequences are highlighted.

where $\mu^{(0,2)}(\underline{s})$ is related to the apparent rupture duration, obtained directly from the apparent source–time function (ASTF) at different stations, and the slowness vector $\underline{s}$ is determined by the seismic phase of interest from a given velocity model, for example the IASP91 (Kennett & Engdahl 1991) model (McGuire *et al.* 2001). We investigated the *P* waves to be consistent with the spectral ratio analysis. The second moments, $\hat{\mu}^{(0,2)}$, $\widehat{\underline{\underline{\mu}}}^{(2,0)}$ and $\widehat{\underline{\mu}}^{(1,1)}$ are estimated following the same procedure detailed in McGuire (2017) and Fan & McGuire (2018).

Second moments lead to the estimation of earthquake finite source properties, including the rupture length (L_c), characteristic rupture duration (τ_c), the characteristic rupture velocity (v_c) and the instantaneous centroid velocity ($\underline{v}_0$) (Silver 1983; McGuire *et al.*

2001). The directivity ratio, which is defined as $|\underline{v}_0|/v_c$, ranges from 0 for a symmetric bilateral rupture to 1 for a unilateral rupture. In general, bilateral ruptures correspond to $|\underline{v}_0|/v_c \leq \sim 0.5$ (McGuire *et al.* 2002). Here, L_c is the maximum eigenvalue of x_c with $\hat{\underline{n}}$ as the unit eigenvector.

$$x_c\,(\hat{\underline{n}}) = 2\sqrt{\hat{\underline{n}}^T \widehat{\underline{\underline{\mu}}}^{(2,0)} \hat{\underline{n}}} \tag{11}$$

$$\tau_c = 2\sqrt{\hat{\mu}^{(0,2)}} \tag{12}$$
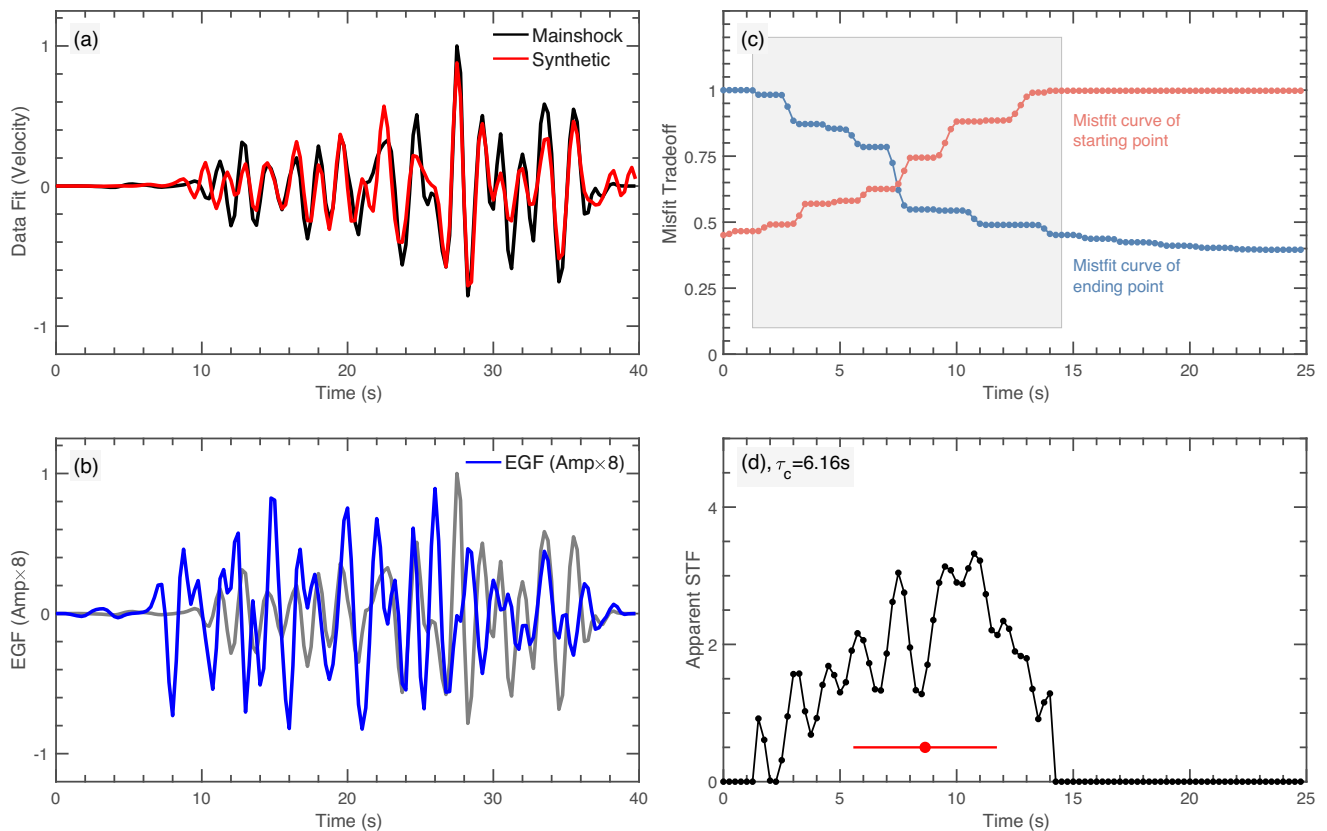
$$v_c = L_c \big/ \tau_c \tag{13}$$

Figure 11. Apparent source–time function deconvolution procedure with the record of 2015A at station INAK as an example. (a) The data fit between the mainshock record and the synthetic seismogram. (b) Corresponding EGF (blue) plotted with the mainshock record (grey). (c) Misfit curves for the ending and starting points of the ASTF. (d) ASTF with its centroid time (red dot) and characteristic rupture duration (red bar).

$$\underline{v}_0 = \widehat{\underline{\mu}}^{(1,1)} \Big/ \hat{\mu}^{(0,2)} \,. \tag{14}$$

In practice, we first obtain *P* waves for the three main 2015 earthquakes and the 29 unique EGFs listed in Table S1 for stations registered in the International Federation of Digital Seismograph Networks (FDSN) within 90° epicentral distance. Seismograms are bandpass filtered between 0.3 and 1 Hz. We discard records with low (<5) signal-to-noise ratios defined as the rms ratio of a 10-s window starting from the IASP91 predicted *P*-wave arrival time and a 10-s window preceding the signal window. With the remaining data, an EGF deconvolution (eqs 6 and 7 in Fan & McGuire 2018) in the time domain is performed to each main shock–EGF pair at a given station (Figs 11A and B). The deconvolution procedure grid-searches starting and ending points (e.g. Fig. 11C) to invert an apparent source–time function (ASTF, e.g. Fig. 11D), in which total duration is prescribed to be less than 25 s (Fan & McGuire 2018). For each master–EGF-station record, we solve for the ASTF that best fits the first 30 s of the master *P* wave. We discard any ASTFs with misfits greater than 50 per cent and calculate $\mu^{(0,2)}(\underline{s})$ for the remaining ASTFs. For example, at station INKA, the apparent duration (τ_c) of 2015A is 6.16 s (Fig. 11D). In total, 32 $\mu^{(0,2)}(\underline{s})$ were used to invert the second moments of 2015A, and 29 and 33 were used for 2015B and 2015C, respectively (Fig. 12, Figs S3–S5).

Good azimuthal coverage of the measurements is needed to capture the directivity of apparent durations to infer the rupture kinematics. We initially attempted the second moments analysis using

only the preferred master–EGF pairings. However, this limited azimuthal coverage produced insufficient measurements and an unstable inversion. By using all the EGFs, we even out the influences of the outliers and stabilize the inversion. For our spectral ratio analysis, there is no quantitative measure of EGF quality, which is why we apply distance constraints. The misfit criteria in the second moments analysis is a quantitative measure of EGF quality. Only good EGFs can produce a decent waveform fit thereby allowing us to relax the EGF distance criteria.

Following Fan & McGuire (2018, see eq. 8 in reference), we solve for the second moments using the complete apparent duration data (Model I) and an interpolated data set (Model II) respectively. Since second moments are spatially smooth (McGuire & Kaneko 2018), we fit 3rd degree polynomials to the sets of apparent duration observations to reduce the variabilities of the scattered $\mu^{(0,2)}(\underline{s})$ measurements (Fig. 12) and then predict apparent durations (Model II interpolated data) for the stations to be used in the inversion. As shown in Fig. 12, the observed apparent durations have a large scatter for all three earthquakes, reflecting the challenges posed by limited usable datasets without any near-field observations. The interpolation helps mitigate the effects of outliers on the second moments solution. Apparent duration predictions from both models agree well with each other sharing similar function forms. This further confirms the interpolation procedure (Fig. 12).

Solutions using the full (Model I) and interpolated (Model II) data indicate that characteristic rupture length and rupture velocity increase with distance from the tear, although the magnitude of these trends vary with the data used for the inversions. The full
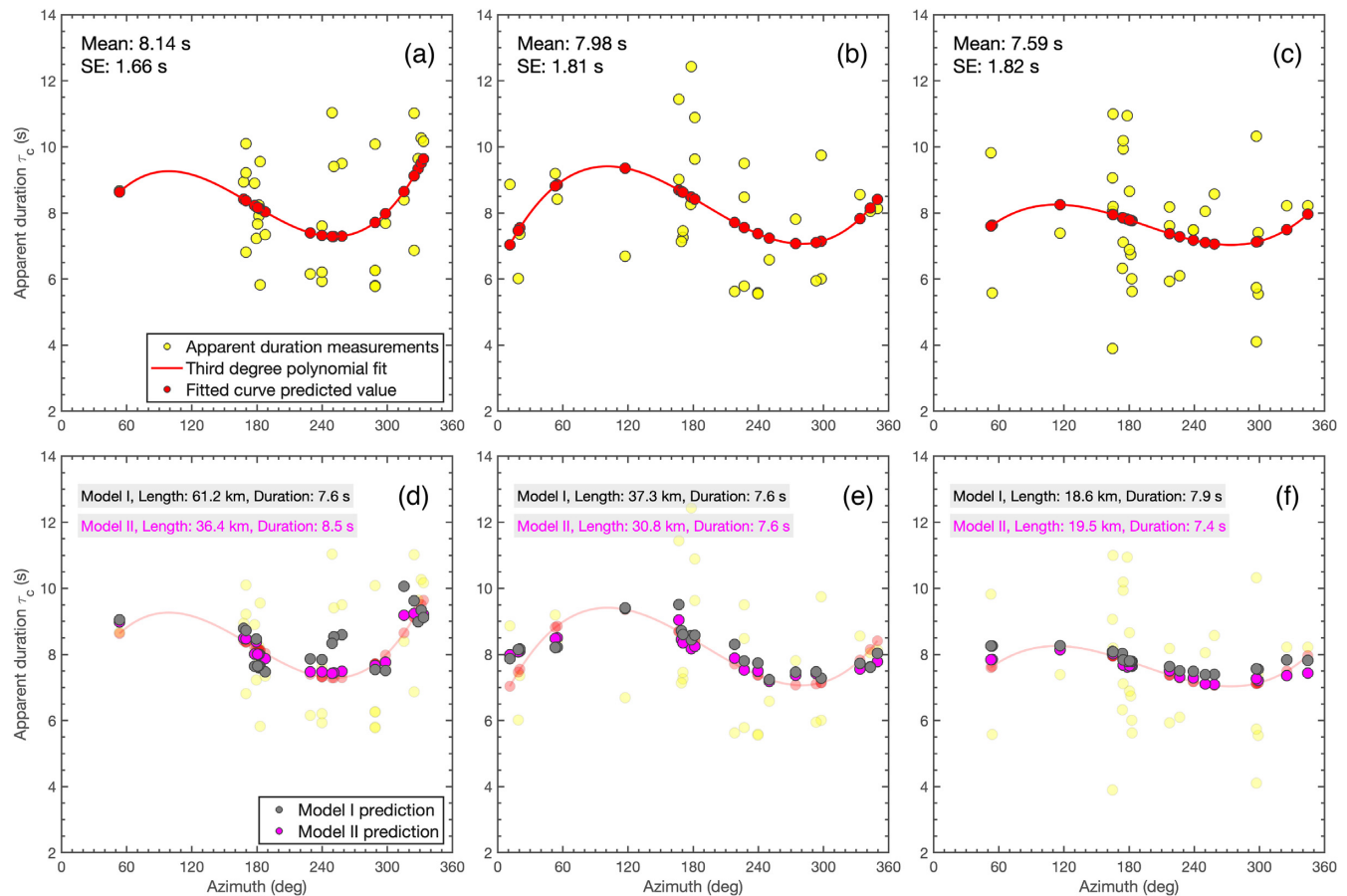
Figure 12. Second moments results. Top panel: apparent duration estimates for 2015A (a), 2015B (b) and 2015C (c) versus azimuth. The mean apparent duration and standard error (SE) of the apparent durations are shown in the upper left-hand corner. Measured values are shown as yellow dots and 3rd degree polynomial fitted values shown as red line and red dots. Bottom panel: predicted apparent durations, characteristic rupture durations, and characteristic rupture lengths for 2015A (d), 2015B (e) and 2015C (f). Model I is based on full data set. Model II is from fitted 3rd degree polynomial.

data inversion (Model I) results indicate that characteristic rupture length (L_c) increases with distance from the tear, from 19 km for 2015C to 37 km for 2015B and 61 km for 2015A (Table 3, Fig. 12). Estimated characteristic rupture durations (τ_c) are similar (~ 8 s) for all three earthquakes. Considering the large differences in rupture length, the similar rupture durations indicate considerable variation in the characteristic rupture velocity (v_c) with values ranging from 8.0 km s^{-1} for 2015A to 2.4 km s^{-1} for 2015C. The interpolated data model (Model II) shows a smaller increase in characteristic rupture length with distance from the tear although 2015A's characteristic rupture length is still almost twice as long as 2015C's (2015A: 36 km; 2015B: 31 km; 2015C: 19 km, Table 3, Fig. 12). Model II suggests that 2015A has a slightly longer rupture duration (8.5 s) than 2015B and 2015C (~ 7.5 s). Rupture velocity increases with distance from the tear (2015A: 4.3 km s^{-1}; 2015B: 4.1 km s^{-1}; 2015C: 2.6 km s^{-1}) although the range of values is not as large as Model I. The directivity ratios from both Model I and Model II suggest that all three earthquakes ruptured bilaterally (Table 3).

Stress drops calculated from the second moments analysis show a decrease in stress drop with distance from the tear (Table 3). Assuming an elliptical fault with length and width defined by the characteristic rupture lengths and widths, we use eq. (5) to estimate stress drops. The rupture width is the second largest eigenvalue of the second spatial moment tensor, and it is less well resolved for the 2015 earthquakes because of the lack of near-field data. For

instance, the estimated width of the 2015C earthquakes is around 3 km, which leads to a stress-drop estimate greater than 400 MPa. Such values might not be accurate on an absolute scale, but are consistent for the 2015 earthquakes because we applied the same approach for all three events. Assuming the resolved rupture widths are representative for the three earthquakes, both Model I and Model II indicate decreasing stress drop with distance from the tear with 2015C having the largest stress drop followed by 2015B and 2015A (Table 3).

The second moments estimates of characteristic rupture velocities also allow for a re-estimation of the rupture area and stress drop from corner frequency. Using eqs (2) and (4), we re-estimate rupture area and stress drop assuming a Brune model and circular fault (Table 4). We assume that rupture velocity (v_r) is half of the characteristic rupture velocity (this assumes a bilateral rupture) and make the following substitution: $\beta = v_r / 0.9$. Using the Model I rupture velocities, both the EGF stack and full stack methods still indicate an increase in rupture length with distance from the tear (Table 4). 2015C has the smallest diameter (~ 30 km) followed by 2015B (35–40 km) and 2015A (50–55 km). The corresponding stress drop estimates indicate a two orders of magnitude decrease in stress drop with distance from the tear from 2015C (~ 55 MPa) to 2015A (~ 0.5 MPa). The results from Model II show similar increasing rupture diameter and decreasing stress drop trends with

Table 3. Second moments results for the 2015 sequence.

Model I

Event	Length (km)	Width (km)	Duration (s)	v_c (km s^{-1})	v_0 (km s^{-1})	v_0/v_c	Ellip. $\Delta\sigma$ (MPa)
2015A	61.2	9.1	7.6	8.0	2.7	0.3	10.0
2015B	37.3	3.9	7.6	4.9	0.6	0.1	152.7
2015C	18.6	2.9	7.9	2.4	0.4	0.2	406.3
Model II							
2015A	36.4	3.2	8.5	4.3	1.6	0.4	133.7
2015B	30.8	3.9	7.6	4.1	0.6	0.1	185.5
2015C	19.5	2.5	7.4	2.6	0.3	0.1	480.5

Table 4. Corner frequency based estimates of rupture diameter and stress drop using rupture velocities from the second moments analysis. 2σ uncertainties indicated.

	Model I		Model II	
	Circ. diam. (km)	Circ. $\Delta\sigma$ (MPa)	Circ. diam. (km)	Circ. $\Delta\sigma$ (MPa)
Event: 2015A				
EGF stack	$51.6^{+7.4}_{-5.8}$	$0.5^{+0.2}_{-0.2}$	$27.5^{+4.0}_{-3.1}$	$3.3^{+1.4}_{-1.1}$
Full stack (fixed slope)	$54.5^{+6.2}_{-5.0}$	$0.4^{+0.1}_{-0.1}$	$29.1^{+3.3}_{-2.7}$	$2.8^{+0.9}_{-0.8}$
Event: 2015B				
EGF stack	$30.3^{+5.4}_{-4.0}$	$4.2^{+2.2}_{-1.7}$	$25.0^{+4.5}_{-3.3}$	$7.4^{+3.9}_{-2.9}$
Full stack (fixed slope)	$27.8^{+3.0}_{-2.5}$	$5.5^{+1.8}_{-1.5}$	$23.0^{+2.5}_{-2.1}$	$9.7^{+3.1}_{-2.6}$
Event: 2015C				
EGF stack	$12.2^{+2.6}_{-1.8}$	$47.0^{+29.4}_{-20.7}$	$13.5^{+2.9}_{-2.0}$	$34.8^{+21.8}_{-15.3}$
Full stack (fixed slope)	$11.1^{+1.5}_{-1.2}$	$62.5^{+25.2}_{-19.9}$	$12.3^{+1.7}_{-1.3}$	$46.2^{+18.7}_{-14.7}$

distance from the tear; however, the magnitudes of the trends are less pronounced (Table 4).

6 DISCUSSION

Using omega-square Brune and Boatwright spectral models, we find the corner frequencies of the 2015 sequence decrease slightly with distance from the tear (Fig. 7) regardless of stacking methodology. Since corner frequency is inversely proportional to rupture duration, a decrease in corner frequency may be due to either an increase in rupture length or a decrease in rupture velocity for earthquakes with similar magnitudes. Assuming a constant rupture velocity for the 2015 master events, we find that rupture length increases with distance from the tear in (Fig. 8, Table 2), although the choice of spectral ratio stacking methods and spectral models influences the magnitude of this trend. We also observe an increase in earthquake rupture length and an increase in the mean of apparent duration with distance from the tear from the second moments analysis (Fig. 12). The Model I and Model II second moments characteristic rupture lengths are shorter than the elliptical rupture lengths estimated from the EGF and full stack methods (using a fixed rupture velocity) except for the Model I estimate for 2015A, which closely matches the corner frequency results (Tables 2 and 3). Although the magnitude of the increasing rupture length trend varies with methodology, the consistent trend observed from independent analyses suggests that it is robust. Similar corner frequency and second moments analyses by Chen & McGuire (2016) on Mendocino Triple Junction earthquakes also showed that although absolute values may vary, the application of multiple independent methods can highlight interevent variability. Increasing rupture length

is also one plausible explanation for the observed increase in normalized centroid time-delay for the 2015 sequence (Fig. 10). For earthquakes with similar magnitudes, the earthquake with a longer rupture length will have a larger centroid time-delay when the rupture speeds are comparable (Pérez-Campos *et al.* 2003; Duputel *et al.* 2013).

Decreasing rupture velocity could also account for the corner frequency and normalized centroid-time delay trends, although this seems unlikely as the second moments analysis indicates that rupture velocity increases (not decreases) with distance from the tear (Table 3). Previous analyses of rupture velocities of large continental earthquakes also suggest that rupture velocity is more likely to increase (rather than decrease) along mature portions of a fault. Perrin *et al.* (2016) found that during large continental earthquakes, fault sections farthest from the long-term fault propagating tip (i.e. those along more mature fault sections) experience faster rupture velocities (if significant rupture variations are observed) compared to the fault sections closer to the fault propagating tip (i.e. the immature fault sections). In addition, the radiated energy data of the 2015 master events (IRIS DMC 2013) shows that 2015A radiated more high frequency energy (4.59e13 J) than 2015C (3.57e13 J), contradicting the slow rupture velocity hypothesis as a slow rupture radiates less energy at high frequencies than a similarly sized earthquake with normal rupture speeds (Kanamori & Rivera 2006). Therefore, decreasing rupture velocity is not likely the reason for the observed corner frequency decrease and normalized centroid time-delay increase in the 2015 sequence.

Increasing rupture complexity is another plausible explanation for the observed increase in the normalized centroid time-delay (Pérez-Campos *et al.* 2003; Duputel *et al.* 2013). 2015A's deviation from the standard omega-square model suggests that it may be

a complex rupture, similar to observations by Uchide & Imanishi (2016). By allowing the spectral falloff exponent to also vary freely, we estimate a larger spectral falloff exponent and corner frequency for 2015A, which leads to a decrease in the circular rupture diameter from 43 to 27 km and a decrease in the elliptical rupture length from 68 to 26 km (Table 2). 2015A's stress drop also increases to ∼4–5 MPa. 2015A's rupture length and stress drop values estimated via the best-fitting falloff, however, are unlikely to represent the actual source parameters since both the circular and elliptical rupture models assume simple source spectra with a fixed spectral falloff. Both an increase in rupture length or rupture complexity could account for 2015A's relatively large normalized centroid time-delay. However, the second moments analysis favors the varying rupture length hypothesis.

A similar normalized centroid-time delay increase with the 1993 earthquakes suggests that our observed trend may not be a random occurrence. Both 1993A and 2015A, which ruptured similar portions of the SCT farthest from the tear, have the largest normalized centroid time-delays in their respective sequences. The other M_w ∼7 earthquakes that occurred on sections of the SCT closer to the tear have the lowest normalized centroid time-delay values. This repetitious pattern suggests that earthquakes farther from the tear behave systematically differently than those closer to the tear.

Cumulative fault displacement may be driving these along-strike rupture variations. Along the SCT, distance from the tear equates to total cumulative displacement. 2015A occurred ∼80 km farther from the tear than 2015C. This distance–displacement relationship means that 2015A's fault section has experienced ∼80 km more displacement than 2015C's fault section. Likewise, 1993A occurred on a portion of the fault that has experienced ∼70 km more displacement than 1993B's section. In continental strike-slip settings, Wesnousky (1988) observed a reduction in structural complexity with increasing fault displacement. Structural features like fault step overs (Wesnousky 2006) have been found to limit strike-slip earthquake rupture extent and should be reduced with increased displacement. Based on this structural evolution model, we would expect that the consolidation and lengthening of fault segments would lead to longer earthquake rupture lengths and faster rupture speeds as rupture barriers are minimized. Note that an increase in earthquake complexity would appear to run counter to this model, but it is possible that an increase in earthquake complexity may represent an unexpected transient effect of fault evolution. Although more earthquake source observations along the SCT are required to determine whether longer or more complex ruptures are causing the along-strike rupture variations, our observations of two similar earthquake sequences that may represent a complete earthquake cycle support ongoing displacement-driven fault maturation, possibly reflecting a continuation of the SCT's development process observed by Neely & Furlong (2018).

5 CONCLUSION

We have utilized spectral ratio analyses via EGFs to document the rupture properties of a 2015 sequence of propagating strike-slip earthquakes along the SCT. Traditional omega-square spectral models indicate that corner frequency values decrease slightly with distance from the tear, which most likely indicates increasing rupture length. The 2015 earthquake farthest from the tear, however, deviates from the traditional omega-square model, suggesting possible rupture complexity. Our second moments analysis of the 2015

sequences indicates a possible increase in rupture length and rupture speed with distance from the tear. Both an increase in rupture length or complexity may explain the 2015 sequence's increase in normalized centroid-time delay with distance from the tear. A similar centroid-time delay trend for the 1993 earthquake sequence suggests that earthquake rupture varies systematically along the SCT. Since distance from the tear represents total cumulative displacement, the rupture variations of these moderate-to-large strike-slip earthquakes may be further evidence of displacement-driven maturation along the SCT.

REFERENCES

Abercrombie, R.E. 2014. Stress drops of repeating earthquakes on the San Andreas Fault at Parkfield, *Geophys. Res. Lett.,* **41**(24), 8784–8791.

Abercrombie, R.E. 2015. Investigating uncertainties in empirical Green's function analysis of earthquake source parameters, *J. geophys. Res.: Solid Earth,* **120**(6), 4263–4277.

Abercrombie, R.E. & Ekström, G. 2001. Earthquake slip on oceanic transform faults, *Nature,* **410,** 74–77.

Aki, K. 1967. Scaling law of seismic spectrum, *J. geophys. Res.,* **72**(4), 1217–1231.

Aktuğ, B., Doğru, A., Özener, H. & Peyret, M. 2015. Slip rates and locking depth variations along central and easternmost segments of North Anatolian Fault, *Geophys. J. Int.,* **202**(3), 2133–2149.

Allmann, B.P. & Shearer, P.M. 2009. Global variations of stress drop for moderate to large earthquakes, *J. geophys. Res.: Solid Earth,* **114**(B1).

Baltay, A., Prieto, G. & Beroza, G.C. 2010. Radiated seismic energy from coda measurements and no scaling in apparent stress with seismic moment, *J. geophys. Res.: Solid Earth,* **115**(B8).

Baltay, A., Ide, S., Prieto, G. & Beroza, G. 2011. Variability in earthquake stress drop and apparent stress, *Geophys. Res. Lett.,* **38**(6).

Becker, J.J. *et al.* 2009. Global bathymetry and elevation data at 30 arc seconds resolution: SRTM30_PLUS, *Mar. Geod.,* **32**(4), 355–371.

Ben-Zion, Y. & Sammis, C.G. 2003. Characterization of fault zones, *Pure appl. Geophys*., **160**(3), 677–715.

Bilich, A., Frohlich, C. & Mann, P. 2001. Global seismicity characteristics of subduction-to-strike-slip transitions, *J. geophys. res.: Solid Earth,* **106**(B9), 19443–19452.

Boatwright, J. 1980. A spectral theory for circular seismic sources; simple estimates of source dimension, dynamic stress drop and radiated seismic energy, *Bull. seism. Soc. Am.,* **70**(1), 1–27.

Brune, J.N. 1970. Tectonic stress and the spectra of seismic shear waves from earthquakes, *J. geophys. Res.,* **75**(26), 4997–5009.

Chen, X. & McGuire, J.J. 2016. Measuring earthquake source parameters in the Mendocino triple junction region using a dense OBS array: implication for fault strength variations, *Earth planet. Sci. Lett.,* **453,** 276–287.

Davidesko, G., Sagy, A. & Hatzor, Y.H. 2014. Evolution of slip roughness through shear, *Geophys. Res. Lett.,* **41,** 1492–1498.

DeMets, C., Gordon, R.G. & Argus, D.F. 2010. Geologically current plate motions, *Geophys. J. Int.,* **181,** 1–80.

Duputel, Z., Rivera, L., Kanamori, H. & Hayes, G. 2012. W phase source inversion for moderate to large earthquakes, *Geophys. J. Int.,* **189**(2), 1125–1147.

Duputel, Z., Tsai, V.C., Rivera, L. & Kanamori, H. 2013. Using centroid time-delays to characterize source durations and identify earthquakes with unique characteristics, *Earth planet. Sci. Lett.,* **374,** 92–100.

Dziewonski, A.M., Chou, T. & Woodhouse, J.H. 1981. Determination of earthquake source parameters from waveform data for studies of global and regional seismicity, *J. geophys. Res.,* **86**(B4), 2825–2852.

Ekström, G., Nettles, M. & Dziewoński, A.M. 2012. The global CMT project 2004–2010: centroid-moment tensors for 13,017 earthquakes, *Phys. Earth planet. Inter.,* **200–201,** 1–9.

Eshelby, J.D. 1957. The determination of the elastic field of an ellipsoid inclusion, and related problems, *Proc. R. Soc. Lond., A, Math. Phys. Sci.,* **241**(1266), 376–396.

Fan, W. & McGuire, J.J. 2018. Investigating microearthquake finite source attributes with IRIS Community Wavefield Demonstration Experiment in Oklahoma, *Geophys. J. Int*., **214,** 1072–1087.

Govers, R. & Wortel, M. J. R. 2005. Lithosphere tearing at STEP faults: response to edges of subduction zones, *Earth planet. Sci. Lett.,* **236**(1-2), 505–523.

Huang, Y., Beroza, G.C. & Ellsworth, W.L. 2016. Stress drop estimates of potentially induced earthquakes in the Guy-Greenbrier sequence, *J. geophys. Res.: Solid Earth,* **121**(9), 6597–6607.

Huang, Y., Ellsworth, W.L. & Beroza, G.C. 2017. Stress drops of induced and tectonic earthquakes in the central United States are indistinguishable, *Sci. Adv.,* **3**(8).

Ide, S., Beroza, G.C., Prejean, S.G. & Ellsworth, W.L. 2003. Apparent break in earthquake scaling due to path and site effects on deep borehole recordings, *J. geophys. Res.: Solid Earth,* **108**(B5).

Imanishi, K. & Ellsworth, W.L. 2006. Source scaling relationships of microearthquakes at Parkfield, CA, determined using the SAFOD pilot hole seismic array, in *Earthquakes: Radiated Energy and the Physics of Faulting,* Vol. **170,** pp. 81–90, eds Abercrombie, R., McGarr, A., Di, Toro G. & Kanamori, H., American Geophysical Union.

IRIS DMC 2013. Data Services Products: EQEnergy Earthquake energy & rupture duration, doi:10.17611/DP/EQE.1

Kagan, Y.Y., 2007. Simplified algorithms for calculating double-couple rotation, *Geophys. J. Int.,* **171,** 411–418.

Kanamori, H. & Rivera, L., 2006. Energy partitioning during an earthquake, in *Earthquakes: Radiated Energy and the Physics of Faulting,* Vol. **170,** pp. 3–13, eds Abercrombie, R., McGarr, A., Di, Toro G. & Kanamori, H., American Geophysical Union.

Kaneko, Y. & Shearer, P.M. 2015. Variability of seismic source spectra, estimated stress drop, and radiated energy, derived from cohesive-zone models of symmetrical and asymmetrical circular and elliptical ruptures, *J. geophys. Res.: Solid Earth,* **120**(2), 1053–1079.

Kennett, B. L. N. & Engdahl, E.R. 1991. Travel times for global earthquake location and phase association, *Geophys. J. Int*., **105,** 429–465.

Madariaga, R. 1976. Dynamics of an expanding circular fault, *Bull. seism. Soc. Am.,* **66**(3), 639–666.

Madariaga, R. 1977. Implications of stress-drop models of earthquakes for the inversion of stress drop from seismic observations, *Pure appl. Geophys.,* **115**(1-2), 301–316.

MATLAB and Optimization Toolbox Release 2015a. The MathWorks, Inc., Natick, Massachusetts, United States.

Martel, S.J., Pollard, D.D. & Segall, P. 1988. Development of simple strike-slip fault zones, Mount Abbot quadrangle, Sierra Nevada, California , . *Bull. geol. Soc. Am.,* **1000,** 1451–1465.

McGuire, J.J. 2017. A MATLAB toolbox for estimating the second moments of earthquake ruptures, *Seismol. Res. Lett.,* **88**(2A).

McGuire, J.J. & Kaneko, Y. 2018. Directly estimating earthquake rupture area using second moments to reduce the uncertainty in stress drop, *Geophys. J. Int.,* **214**(3), 2224–2235.

McGuire, J.J., Zhao, L. & Jordan, T.H. 2001. Teleseismic inversion for the second-degree moments of earthquake space-time distributions, *Geophys. J. Int.,* **145,** 661–678.

McGuire, J.J., Zhao, L. & Jordan, T.H. 2002. Predominance of unilateral rupture for a global catalog of large earthquakes, *Bull. seism. Soc Am,* **92**(8), 3309–3317.

Mueller, C.S. 1985. Source pulse enhancement by deconvolution of an empirical Green's function, *Geophys. Res. Lett.,* **12**(1), 33–36.

Neely, J.S. & Furlong, K.P. 2018. Evidence of displacement-driven maturation along the San Cristobal Trough transform plate boundary, *Earth planet. Sci. Lett.,* **485,** 88–98.

Perrin, C., Manighetti, I., Ampuero, J-P., Cappa, F. & Gaudemer, Y. 2016. Location of largest earthquake slip and fast rupture controlled by along-strike change in fault structural maturity due to fault growth, *J. geophys. Res.: Solid Earth,* **121,** 3666–3685,

Pérez-Campos, X., McGuire, J.J. & Beroza, G.C. 2003. Resolution of the slow earthquake/high apparent stress paradox for oceanic transform fault earthquakes, *J. geophys. Res.: Solid Earth,* **108**(B9).

Sato, T. & Hirasawa, T. 1973. Body wave spectra from propagating shear cracks, *J. Phys. Earth,* **21,** 415–431.

Shearer, P.M. 2009. *Introduction to Seismology,* 2nd edn, Cambridge University Press.

Silver, P. 1983. Retrieval of source-extent parameters and the interpretation of corner frequency, *Bull. seism. Soc. Am.,* **73**(6), 1499–1511.

Smith-Konter, B. R, Sandwell, D.T. & Shearer, P. 2011. Locking depths estimated from geodesy and seismology along the San Andreas Fault System: implications for seismic moment release, *J. geophys. Res.: Solid Earth,* **116**(B6).

Thomas, A.M., Bürgmann, R. & Dreger, D.S. 2013. Incipient faulting near Lake Pillsbury, California, and the role of accessory faults in plate boundary evolution, *Geology,* **41**(10), 1119–1122.

Uchide, T. & Imanishi, K. 2016. Small earthquakes deviate from the omega-square model as revealed by multiple spectral ratio analysis, *Bull. seism. Soc. Am.,* **106**(3), 1357–1363.

Wechsler, N., Ben-Zion, Y. & Christofferson, S. 2010. Evolving geometrical heterogeneities of fault trace data, *Geophys. J. Int.,* **182**(2), 551–567.

Wells, D.L. & Coppersmith, K.J. 1994. New empirical relationships among magnitude, rupture length, rupture area and surface displacement, *Bull. seism. Soc. Am.,* **84**(4), 974–1002.

Wesnousky, S.G. 1988. Seismological and structural evolution of strike-slip faults, *Nature,* **355,** 340–343.

Wesnousky, S.G. 2006. Predicting the endpoints of earthquake ruptures, *Nature,* **444,** 358–360.

Wessel, P. & Smith, W. H. F. 1991. Free software helps map and display data, *EOS, Trans. Am. Geophys. Un.,* **72**(41), 441–441.

Ye, L., Lay, T., Kanamori, H. & Rivera, L. 2016. Rupture characteristics of major and great (Mw ≥7.0) megathrust earthquakes from 1990 to 2015: 1. Source parameter scaling relationships, *J. geophys. Res.: Solid Earth,* **121**(2), 826–844.

Young, J.B., Presgrave, B.W., Aichele, H., Wiens, D.A. & Flinn, E.A. 1996. The Flinn-Engdahl regionalisation scheme: the 1995 revision, *Phys. Earth planet. Inter.,* **96**(4), 223–297.

SUPPORTING INFORMATION

Supplementary data are available at *GJI* online.

Text S1.
Table S1. Earthquakes used as empirical Green's functions.
Table S2. SCT earthquakes $>M_w$ 6 and GCMT centroid time-delays. The IDs for the 1993 and 2015 sequence earthquakes discussed in this paper are listed in parentheses.
Table S3. W-phase derived normalized centroid time-delay solutions for the 1993 and 2015 earthquake sequences. 1993 sequence data are available from http://wphase.unistra.fr/. 2015 data obtained via personal correspondence with Dr Zacharie Duputel.

Figure S1. Full stack method synthetic tests. We stack spectra across EGFs to ensure that the master corner frequency is recoverable. Top panel: Four Brune spectra with the same master corner frequency but different moment ratios and EGF corner frequencies. Middle: Same spectra with noise added (sampled from a log-normal distribution with standard deviation 0.5). Bottom panel: Stack from all four spectra. The estimated master corner frequency of 0.04 Hz is 0.01 Hz lower than the input master corner frequency (0.05 Hz) but is similar to the synthetic signals with noise. Therefore, the master corner frequency is recoverable using this methodology. This stacking method works for both Brune and Boatwright models if EGF corner frequencies are within ∼1 order of magnitude of each other.

Figure S2. Full stack spectra (free slope) (2015 earthquake sequence) (grey) with best fitting Brune model (red) when falloff exponent is allowed to vary. Note the steeper falloff for 2015A (∼5) compared to 2015B and 2015C (∼2).

Figure S3: 2015A apparent source–time function deconvolution. Panel A: Mainshock and synthetic with station and misfit indicated.

Panel B: EGF (blue) with mainshock (grey). Panel C: Apparent source–time function with centroid time (red dot) and characteristic duration (red line) indicated.

Figure S4: 2015B apparent source–time function deconvolution. Panel A: Mainshock and synthetic with station and misfit indicated. Panel B: EGF (blue) with mainshock (grey). Panel C: Apparent source–time function with centroid time (red dot) and characteristic duration (red line) indicated.

Figure S5: 2015C apparent source–time function deconvolution. Panel A: Mainshock and synthetic with station and misfit indicated. Panel B: EGF (blue) with mainshock (grey). Panel C: Apparent source–time function with centroid time (red dot) and characteristic duration (red line) indicated.

Please note: Oxford University Press is not responsible for the content or functionality of any supporting materials supplied by the authors. Any queries (other than missing material) should be directed to the corresponding author for the paper.